

Tensile-strained growth on low-index GaAs

Cite as: J. Appl. Phys. **112**, 054313 (2012); <https://doi.org/10.1063/1.4749407>

Submitted: 17 January 2012 • Accepted: 09 August 2012 • Published Online: 06 September 2012

Paul J. Simmonds and Minjoo Larry Lee



View Online



Export Citation

ARTICLES YOU MAY BE INTERESTED IN

[Molecular beam epitaxy of metamorphic \$\text{In}_y\text{Ga}_{1-y}\text{P}\$ solar cells on mixed anion \$\text{GaAs}_x\text{P}_{1-x}/\text{GaAs}\$ graded buffers](#)

Journal of Vacuum Science & Technology B **29**, 03C118 (2011); <https://doi.org/10.1116/1.3559119>

[Tensile GaAs\(111\) quantum dashes with tunable luminescence below the bulk bandgap](#)

Applied Physics Letters **105**, 071912 (2014); <https://doi.org/10.1063/1.4893747>

[Metamorphic GaAsP buffers for growth of wide-bandgap InGaP solar cells](#)

Journal of Applied Physics **109**, 013708 (2011); <https://doi.org/10.1063/1.3525599>



Time to get excited.

Lock-in Amplifiers – from DC to 8.5 GHz



Find out more



Tensile-strained growth on low-index GaAs

Paul J. Simmonds^{a)} and Minjoo Larry Lee

Department of Electrical Engineering, Yale University, New Haven, Connecticut 06520-8284, USA

(Received 17 January 2012; accepted 9 August 2012; published online 6 September 2012)

We present a comparative study of the growth of tensile-strained GaP on the four low-index surfaces of GaAs: (001), (110), (111)A, and (111)B. For each surface orientation we outline the growth conditions required for smooth GaAs homoepitaxy. We are able to predict the resulting surface morphology when GaP is deposited onto these four GaAs surfaces by considering the influence of surface orientation on tensile strain relief. GaP deposited on GaAs(001) forms extremely smooth, planar layers. In contrast, the elastic relief of tensile strain on both GaAs(110) and GaAs(111)A leads to the three-dimensional self-assembly of GaP into dislocation-free nanostructures. Similarities between tensile and compressive self-assembly suggest that the kinetics governing many aspects of self-assembled growth is independent of the sign of strain. We show that differences in self-assembly on GaAs(110) and (111)A are the result of unequal adatom diffusion lengths. Tensile-strained self-assembly also occurs on GaAs(111)B, although our use of misoriented substrates resulted in the formation of one-dimensional nanoscale wires. Tensile-strained self-assembly is a versatile, reliable technique that can be extended to a wide range of materials in order to create dislocation-free nanostructures on (110) and (111) surfaces. © 2012 American Institute of Physics. [<http://dx.doi.org/10.1063/1.4749407>]

I. INTRODUCTION

During the growth of biaxially strained materials, plastic processes (e.g., dislocation nucleation and glide) compete with elastic processes (e.g., surface roughening) to relax the strain.¹ For a specific application one often tries to promote one or the other of these two strain relief mechanisms during material growth. For example, plastic relaxation is encouraged during the growth of metamorphic buffers,² while purely elastic strain relief is required to drive quantum dot self-assembly^{3–5} since mid-gap states associated with dislocation cores adversely affect a dot's optoelectronic properties. The ability to select plastic or elastic deformation as the leading strain relief mechanism is hence of great importance.

Whether elastic or plastic strain relief occurs in III-V epitaxial materials is strongly correlated with the sign of the strain (i.e., tensile or compressive) and the crystallographic orientation of the growth surface.^{6,7} Compressive strain is relatively well understood; on (001) surfaces it is initially relieved elastically, which has been long exploited to create the functional quantum dots described above. On (110) and (111) surfaces compressively strained materials behave very differently, typically undergoing plastic relaxation via dislocation nucleation and glide and forming two-dimensional (2D) layers.^{4,8} We must however also consider material systems under high biaxial strain in order to build a complete picture of the effect of surface orientation on strain relaxation. A comprehensive study of tensile-strained growth on low-index surfaces is hence of fundamental scientific interest but, as we will show, also provides a foundation for the rou-

tine growth of self-assembled nanostructures on (110) and (111) surfaces of III-V materials.

In this paper we present an investigation into the influence of substrate orientation on surface morphology in tensile-strained III-V materials: in particular, tensile-strained GaP grown on the (001), (110), (111)A, and (111)B surfaces of GaAs. We explain why dislocation-free self-assembly occurs on both (110) and (111) surfaces but why we do not see corresponding GaP nanostructures on (001). We identify characteristics that tensile self-assembly on (110) and (111) surfaces shares with the well established self-assembly of compressive materials on (001) surfaces.

II. ELASTIC VS. PLASTIC STRAIN RELIEF

In this section we discuss how the interplay between the sign of strain and the surface orientation allows us to select between elastic and plastic strain relief during material growth.

Biaxial strain, σ , in diamond cubic and zinc blende materials can be resolved into a uniaxial shear stress, τ , on a {111} dislocation glide plane.⁹ The direction of τ is antiparallel in systems under tensile and compressive biaxial strain [Fig. 1(a)].⁹ Atoms on the {111} glide plane experience a shear force due to τ , and it is the irreversible translocation of these atoms from their equilibrium positions that gives rise to the formation of dislocations and stacking-faults. A “total” dislocation occurs when the dislocation Burgers vector, \mathbf{b} , corresponds to the movement of atoms between equivalent lattice positions: for example from a “B” type site to a neighboring “B” type site, as shown in Fig. 1(b).⁹

$\mathbf{a}/2\langle 101 \rangle$ total dislocations are most commonly encountered in III-V materials, and are referred to as 60° dislocations because of the angle formed on the {111} glide plane between the line direction and Burgers vector [Fig. 1(b)].

^{a)}Author to whom correspondence should be addressed. Electronic mail: p.j.simmonds.03@cantab.net. Current address: California NanoSystems Institute, University of California, Los Angeles, California 90095-7227, USA.

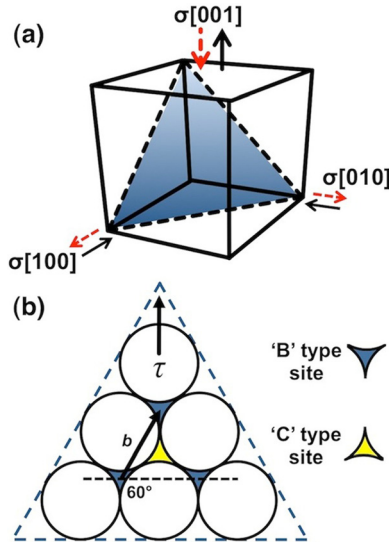


FIG. 1. (a) The addition of a hydrostatic stress tensor converts a biaxial stress state ($\sigma[100] = \sigma[010]$, $\sigma[001] = 0$) into a uniaxial stress, ($\sigma[100] = \sigma[010] = 0$, $\sigma[001] \neq 0$),⁹ as shown schematically for (001)-oriented material under both biaxial compression (black, solid arrows) and biaxial tension (red, dashed arrows). The shaded triangle shows the position of a $\{111\}$ glide plane. (b) Schematic diagram of part of a $\{111\}$ glide plane showing resolution of the uniaxial stress $\sigma[001]$ into a shear stress τ for the case of compressive strain on a (001) surface. White circles represent atoms on “A” type sites. The 60° angle between the Burgers vector, b , and the line direction (dashed) is shown.

A 60° total dislocation will dissociate slightly into a pair of 30° and 90° Shockley partial dislocations as it glides; the net energy of the two partials can be as much as one third lower than that of the 60° total dislocation.¹⁰ The 30° and 90° partial dislocations are bound by a narrow stacking-fault “ribbon” [Fig. 2(a)].¹¹ The passage of a Shockley partial creates a transient stacking-fault by definition, since its Burgers vector does not correspond to a lattice translation vector.

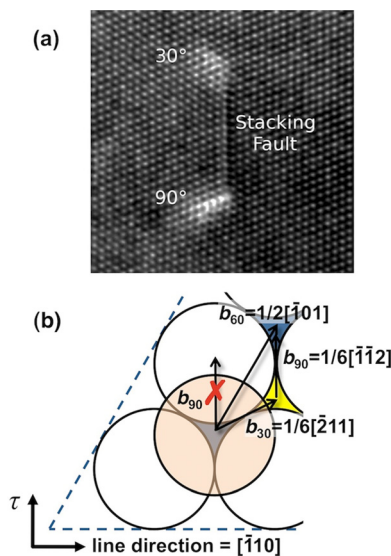


FIG. 2. (a) High-resolution TEM along $\langle 110 \rangle$ showing a narrowly dissociated 60° dislocation in a zinc blende semiconductor. A stacking-fault ribbon connects the cores of the 30° and 90° partial dislocations. (b) Schematic diagram corresponds to the lower-left portion of Fig. 1(b). The shaded circle represents an atom on a “B” type site that moves during dislocation glide.

There is an explicitly defined sequence in which the partials of a dissociated total dislocation must pass. One leads and the other trails in order to maintain close packing. According to the model for plastic deformation proposed by Kvam and Hull, the order in which the two partial dislocations pass is dictated by the combination of the sign of the strain and the orientation of the substrate.⁹ For several strain/orientation combinations below we discuss which partial will lead and how this gives rise to different outcomes for strain relief. In particular, we identify those tensile strained systems for which elastic strain relief dominates and that are therefore conducive to dislocation-free self-assembly.

A. Dislocation behavior for biaxial compression on (001)

Fig. 2(b) represents a small section of a $\{111\}$ glide plane in a compressively strained material grown on a (001) substrate. We see that to prevent the creation of a high-energy A|A stacking fault, the 90° partial is forbidden from leading.⁹ Instead the 30° partial leads, creating a transient, lower-energy A|C stacking-fault. The Burgers vector of the trailing 90° partial, b_{90} , is parallel to the resolved shear stress, τ , on the $\{111\}$ plane. The 90° partial is thus pushed against the 30° partial to complete the motion of the total 60° dislocation and maintain A|B stacking. Hence, for compressively strained material on (001) substrates, the intermediate ribbon is prevented from widening into a stacking-fault.¹² Fig. 2(b) shows that in this case the two partials are forced to behave as a single, high-energy 60° total dislocation, such that $a/2[-101] = a/6[-211] + a/6[-1\bar{1}2]$. The Kvam-Hull model therefore predicts that plastic deformation in compressively strained material on (001) will occur via the nucleation and glide of 60° dislocations.⁹ However, although the formation of these 60° dislocations is allowed, in practice their nucleation is kinetically limited.^{12–14} 60° dislocation nucleation energies (E_{nuc60°) as large as 10–100 eV have been estimated in $\sim 4\%$ compressively strained material on (001).¹⁴ Since the nucleation rate is proportional to $\exp[-E_{nuc60^\circ}/kT]$, such high values for E_{nuc60° lead to an extremely low 60° dislocation nucleation rate over a wide range of growth conditions.¹⁴ The delayed onset of dislocation nucleation under these conditions means that elastic strain relief by surface roughening can take place more quickly. The result is the well-documented self-assembly of dislocation-free nanostructures from compressively strained materials on a (001) surface.^{3–5}

B. Dislocation behavior for biaxial tension on (001)

Fig. 1(a) shows that reversing the sign of biaxial strain from compression to tension inverts the direction of τ on the $\{111\}$ glide plane. From Fig. 3(a) we see that for the scenario of tensile strain on (001), the 90° partial will not only now lead but, since it is parallel to τ , will also experience greater resolved shear stress than either the 30° partial or the 60° total dislocation.

Moreover, for this combination of strain and surface orientation, the 90° partial has a higher Schmid factor than the

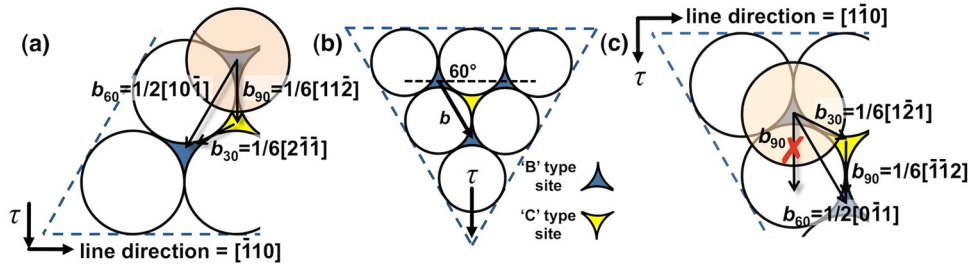


FIG. 3. (a) Schematic diagram corresponding to the lower-left portion of Fig. 1(b) for tensile-strained material on a (001) surface. (b) Schematic diagram showing inverted τ and rotation of the $\{111\}$ glide plane for the case of tensile strain on either a (110) or (111) surface. (c) Schematic diagram corresponding to the upper-left portion of (b). A leading 90° Shockley partial would lead to a high-energy A|A stacking-fault and is therefore highly unlikely. The 30° partial thus leads, followed quickly by the 90° partial.

60° total dislocation; if we normalize to $|b|$, a 90° partial has lower self-energy and a larger strain-relieving component than a 60° total. The two Shockley partials can hence quickly become widely dissociated, with a large stacking-fault formed between them. The higher Schmid factor also means that E_{nuc90° is significantly lower than E_{nuc60° .¹³ Wegscheider and Cerva considered nucleation energies in SiGe, and for a lattice mismatch of 4% found E_{nuc90° to be $\sim 7\times$ smaller than E_{nuc60° (Ref. 13); a similar trend is expected to hold for III-V materials. Since the dislocation nucleation rate is proportional to $\exp[-E_{nuc90^\circ}/kT]$, strain is rapidly relieved by plastic deformation. Tensile-strained materials on (001) surfaces hence typically form flat, heavily dislocated layers with a high density of stacking-faults.^{4,8}

C. Dislocation behavior for biaxial tension on (110) and (111)

Moving from a (001)-oriented surface to either a (110) or a (111) substrate is an equivalent rotation operation in terms of the Thompson tetrahedron.¹¹ As in Sec. II B, τ is inverted for tensile strain (compared with compressive strain) but now the $\{111\}$ glide plane is also rotated [Fig. 3(b)]. A qualitative comparison of Fig. 1(b) and Fig. 3(b) shows them to be symmetrically equivalent. This equivalency is borne out by the dislocation behavior predicted by Kvam and Hull for tensile strain on a (110) or (111) surface. As for the case of compressive strain on (001), 90° partials are forbidden from leading to avoid the formation of high energy A|A stacking-faults [Fig. 3(c)]. The 30° partial hence leads, followed swiftly by the 90° partial which is parallel to τ , and once more the two partials are forced to behave as a single, high-energy 60° total dislocation. Plastic deformation for tensile-strained materials on either a (110) or (111) surface is hence predicted to take place via the nucleation and glide of 60° dislocations.⁹ So, in terms of which partial leads, dislocation behavior for tensile strain on (110) or (111) is identical to that of compressive strain on (001).⁹ By analogy we suggest that the large values of E_{nuc60° in compressively strained material on (001) are similarly high in tensile-strained material on (110) and (111). As before, large values for E_{nuc60° will result in the delayed onset of 60° dislocation nucleation creating an opportunity for elastic deformation to initiate the strain relief, and hence for dislocation-free self-assembly to occur.^{6,7}

III. EXPERIMENT

To test the predictions from Sec. II, we deposited tensile-strained GaP onto homoepitaxial GaAs buffers with (001), (110), (111)A, and (111)B orientations. The tensile strain in the GaP created by the lattice mismatch with GaAs is 3.7%. Crystal growth was carried out in a VEECO MOD GEN II solid-source molecular beam epitaxy (MBE) system using high purity sources of Ga, P₂ and either As₂ or As₄ as detailed in Sec. III A. Beam equivalent pressures (BEP) were determined using a beam flux monitor at the substrate location, while substrate temperatures (T_{sub}) were measured by optical pyrometry. The sticking coefficient of Ga adatoms on (110) and (111) surfaces is assumed to be unity for the range of T_{sub} used in this study.¹⁵ Growth rates in monolayers per second on (110) and (111) were hence calculated by measuring reflection high-energy electron diffraction intensity oscillations on GaAs(001) and correcting for the areal density of available lattice sites on the (110) and (111) surfaces. To analyze sample surface morphology post-growth we used a DIGITAL INSTRUMENTS atomic force microscope (AFM) in tapping mode. Using a TECNAI F20 operated at 200 kV, we performed cross sectional transmission electron microscopy (XTEM) to observe internal strain-contrast in our samples.

A. Homoepitaxial GaAs growth conditions

The MBE conditions necessary to grow high-quality homoepitaxial GaAs buffers vary with substrate orientation. We based our choice of conditions on a review of the literature (for example, references cited in this section and references therein).

For GaAs(001) substrates (on-axis $\pm 0.5^\circ$) we performed an initial 30 min degas at $T_{\text{sub}} = 650^\circ\text{C}$, before growth of GaAs buffers at $T_{\text{sub}} = 590^\circ\text{C}$, at a growth rate of $1.0 \mu\text{m/h}$ and with an As₂/Ga BEP ratio ~ 25 .

During GaAs(110) homoepitaxy As₄ is preferred over As₂,¹⁶ and a high As₄ flux combined with reduced T_{sub} is known to help prevent faceted growth.^{16,17} We degassed GaAs(110) substrates (on-axis $\pm 0.5^\circ$) for 20 min at $T_{\text{sub}} = 610^\circ\text{C}$, before growing 60 nm GaAs buffers at $T_{\text{sub}} = 540^\circ\text{C}$, at a growth rate of $0.45 \mu\text{m/h}$ and with an As₄/Ga BEP ratio ~ 75 . Following growth we annealed the GaAs(110) buffers at $T_{\text{sub}} = 600^\circ\text{C}$ for 15 min to promote surface smoothing.

There is a shortage of literature on growing smooth homoepitaxial GaAs(111)A. For a wide range of MBE

conditions, GaAs growth results in the formation of pyramidal defects across the buffer surface.¹⁸ It has been shown however that use of a high As_4/Ga BEP ratio¹⁵ can help suppress formation of these undesirable 3D features. We degassed nominally on-axis ($\pm 0.5^\circ$) GaAs(111)A substrates for 30 min at $T_{\text{sub}} = 630^\circ\text{C}$. We then grew 60 nm GaAs buffers at $T_{\text{sub}} = 540^\circ\text{C}$, at a growth rate of $0.45\ \mu\text{m}/\text{h}$ and with an As_4/Ga BEP ratio ~ 70 . Following growth we annealed the GaAs(111)A buffers at $T_{\text{sub}} = 640^\circ\text{C}$ for 15 min to promote surface smoothing.

Similar issues with pyramidal defect formation during GaAs(111)B homoepitaxy have led to the adoption of misoriented substrates on which smooth GaAs layers can be grown.¹⁹ We used GaAs(111)B substrates off-cut by 2° towards $\langle 110 \rangle$, which we degassed for 10 min at $T_{\text{sub}} = 615^\circ\text{C}$. We then grew 60 nm GaAs buffers at $T_{\text{sub}} = 600^\circ\text{C}$, at a growth rate of $0.45\ \mu\text{m}/\text{h}$ and with an As_2/Ga BEP ratio ~ 70 (although we also achieved GaAs(111)B homoepitaxy of equally high quality using As_4 instead). Following growth we annealed the GaAs(111)B buffers at $T_{\text{sub}} = 610^\circ\text{C}$ for 1 h to promote surface smoothing.

Using the optimized growth conditions outlined above, we could consistently prepare homoepitaxial GaAs buffers, flat on the scale of the monolayer step height, for all four surface orientations [Fig. 4]. Root mean square (rms) roughness, measured over a $225\ \mu\text{m}^2$ area on each buffer type, ranged from 0.27 nm for GaAs(001) to 0.70 nm for GaAs(111)B. The relatively wide terraces on the nominally on-axis (001), (110), and (111)A surfaces [Figs. 4(a)–4(c)] contrast strongly with the high density of step-edges induced by the misorientation of the (111)B substrate [Fig. 4(d)].

B. Growth of GaP on GaAs

Following growth of GaAs buffers with each of the four orientations described above, we reduced T_{sub} to the temperature required for GaP deposition: 460°C for GaAs(001) and GaAs(110), 520 – 580°C for GaAs(111)A and 460°C for GaAs(111)B. The valve of the arsenic cracker cell was closed for 20 s to limit the amount of excess surface As

atoms present at the start of the GaP growth. We then opened Ga and P_2 simultaneously to deposit 0.0–6.4 ML GaP, at growth rates from 0.014–0.142 ML/s and with a P_2/Ga BEP ratio ~ 10 , before cooling immediately under P_2 .

IV. RESULTS AND DISCUSSION

A. Tensile-strained growth on GaAs(001)

The deposition of 4.5 ML GaP onto GaAs(001) resulted in an extremely flat surface morphology, with no self-assembled 3D features [Fig. 5(a)]. The rms roughness measured across $225\ \mu\text{m}^2$ was $< 0.5\ \text{nm}$, which is comparable to that of the underlying GaAs(001) buffer. From Sec. II B we anticipate that relief of biaxial tension on a (001) surface will be led by plastic rather than elastic deformation. The absence of elastic surface roughening or self-assembly in Fig. 5(a) is in keeping with this prediction. However, when viewed using XTEM we saw no evidence of plastic dislocation formation within the 4.5 ML GaP layer [Fig. 5(b)]. During the growth of tensile strained Si on Ge(001) (with a similar lattice mismatch of $\sim 3.8\%$), Pachinger *et al.* reported that planar, dislocated wetting layers could be grown up to 8 ML thick, before a transition to disordered 3D growth occurred.⁸ We hence anticipate that thicker layers of GaP on GaAs(001) will be needed in order to observe the expected strain relief by plastic deformation.

B. Tensile-strained growth on GaAs(110) and GaAs(111)A

Codeposition of Ga and P_2 onto the surface of both GaAs(110) and GaAs(111)A results in the self-assembly of discrete, 3D nanostructures [Fig. 6]. The 3D, tensile-strained nanostructures self-assemble in the absence of a wetting layer via the Volmer-Weber (VW) growth mode for both GaP/GaAs(110) and GaP/GaAs(111)A. The VW mode is

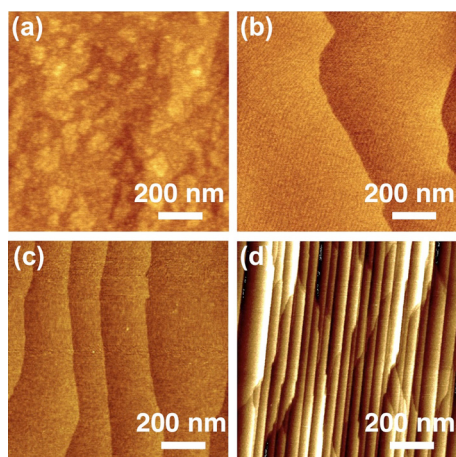


FIG. 4. $1\ \mu\text{m}^2$ AFM images of homoepitaxial GaAs buffers grown on (a) GaAs(001), (b) GaAs(110), (c) GaAs(111)A, and (d) GaAs(111)B substrates showing the orientation dependence of the monolayer terrace morphology. The z-scale in each image is 3 nm.

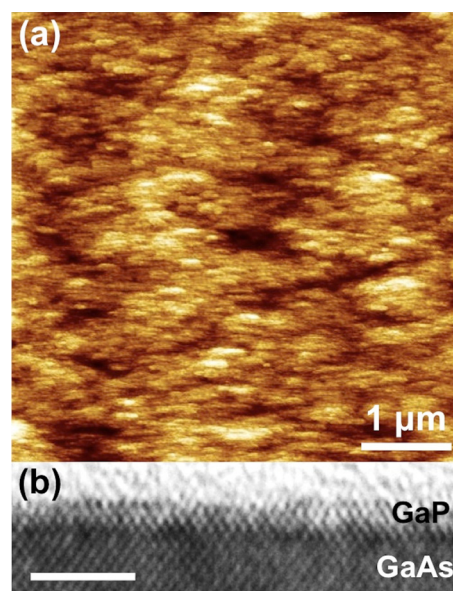


FIG. 5. Microscopy of 4.5 ML GaP/GaAs(001): (a) $25\ \mu\text{m}^2$ AFM image showing a highly planar, 2D surface morphology (z-scale = 2 nm); (b) high-resolution XTEM image of the 4.5 ML GaP surface layer (scale bar represents 5 nm).

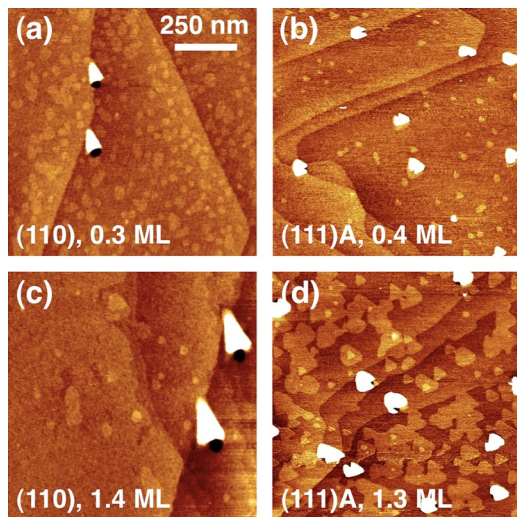


FIG. 6. $1 \mu\text{m}^2$ AFM images comparing the surface morphologies of (a) 0.3 ML GaP/GaAs(110) ($T_{\text{sub}} = 460^\circ\text{C}$), (b) 0.4 ML GaP/GaAs(111)A ($T_{\text{sub}} = 580^\circ\text{C}$), (c) 1.4 ML GaP/GaAs(110) ($T_{\text{sub}} = 460^\circ\text{C}$), and (d) 1.3 ML GaP/GaAs(111)A ($T_{\text{sub}} = 580^\circ\text{C}$). The z-scale in each image is 3 nm.

frequently explained in terms of capillarity arguments and occurs when $\gamma_s < \gamma_e + \gamma_i$, where γ_s , γ_e , and γ_i are the free energies of the substrate/vacuum, epilayer/vacuum, and substrate/epilayer interfaces, respectively.⁴ Assuming that $\gamma_i \geq 0$, VW growth of GaP on GaAs will occur so long as $\gamma_{\text{GaAs}} < \gamma_{\text{GaP}}$ and from literature values for both (110) and (111) we find this to be the case.²⁰ GaAs(110) and (111)A both exhibit 3D self-assembly long before a complete monolayer of GaP has been deposited [Figs. 6(a) and 6(b)]. A continuous GaP wetting layer cannot therefore be present and this is a signature of VW growth. Tensile strained VW growth contrasts with the Stranski-Krastanov (SK) mode typically observed during compressively strained self-assembly.^{5,21} Although surface energy and the magnitude of the strain both affect which of these 3D growth modes occur, it is noteworthy that the only report of tensile-strained self-assembly in Group IV materials also found VW growth.²² It is hence possible that the *sign* of strain may be a third factor influencing the growth mode.

Capillarity arguments alone are however, insufficient to explain the disparate strain-relief behavior we observe: i.e., 2D planar growth for GaP on GaAs(001) [Fig. 5(a)]; and 3D self-assembly GaP on GaAs(110) and GaAs(111)A [Fig. 6]. The ratio $\gamma_{\text{GaP}}/\gamma_{\text{GaAs}}$ for each of the (001), (110), and (111) orientations is 1.32, 1.33, and 1.31, respectively.²⁰ Despite similar relative surface energies, we have seen that tensile strain relief occurs very differently on the three surfaces. These differences indicate that, as discussed in Sec. II, it is the combination of sign of strain and surface orientation that governs whether plastic or elastic relaxation takes place.

GaP nanostructures on GaAs(110) and GaAs(111)A exhibit monomodal size distributions regardless of the deposition thickness,^{6,7} with no evidence of the Ostwald ripening common in compressively strained self-assembly.²³ In the future, the low size dispersion we see in tensile-strained self-assembly could be used to create the highly uniform quantum dot arrays which are needed for optoelectronic devices with a narrow spectral bandwidth.²⁴

Another appealing aspect of tensile strained self-assembly is predictable control over nanostructure formation. Straightforward adjustments to GaP deposition thickness,^{6,7} deposition temperature,⁷ and deposition rate allow us to accurately manipulate the height, diameter, and areal density of nanostructures on both GaAs(110) and GaAs(111)A. For example, varying the deposition rate of 0.7 ML GaP on GaAs(110) between 0.014 and 0.142 ML/s allowed us to tune the nanostructure density from 5×10^6 – $7 \times 10^7 \text{ cm}^{-2}$ [Fig. 7]. Although the dashed guide-to-the-eye in Fig. 7 suggests a linear dependence rate over this range, additional data points will be needed to confirm this quantitatively. These areal densities (and those on GaP/GaAs(111)A)⁷ are orders of magnitude lower than the values of 10^9 – 10^{11} cm^{-2} typical for compressively strained (001) self-assembly.²¹ Nanostructure arrays with areal densities $\sim 10^7 \text{ cm}^{-2}$ are highly desirable for applications such as single-photon emission.²⁵ The significantly lower areal density seen in tensile-strained self-assembly compared with canonical compressive self-assembly on (001) substrates is almost certainly due to larger adatom diffusion lengths on the (110) and (111) surfaces.²⁶ We consider the topic of adatom diffusion length in more detail in Sec. IV C.

The response of nanostructure size and density to changes in growth conditions during tensile-strained self-assembly corresponds closely with established trends in traditional, compressively strained self-assembly. The influence of T_{sub} , V/III BEP ratio, and growth rate are well understood in compressive systems,⁴ and these variables have the same general effects on tensile-strained GaP/GaAs(110) and GaAs(111)A self-assembly.^{6,7} For example, the trend of increasing areal density with growth rate in [Fig. 7] has long been reported in compressive systems.²⁷ Ga adatom migration is known to reduce at higher growth rates so that on average each stable cluster of adatoms forms more quickly.

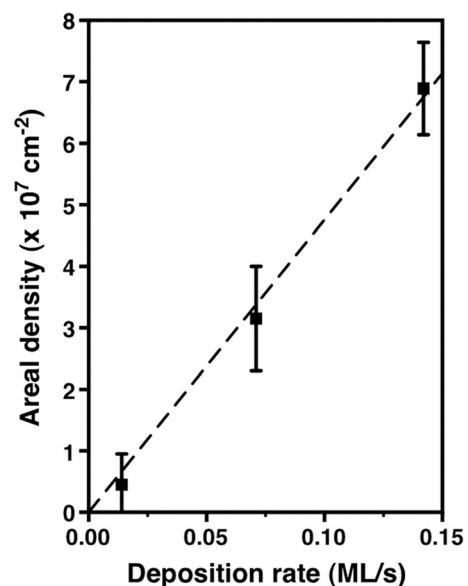


FIG. 7. Nanostructure areal density as a function of GaP deposition rate for samples of 0.7 ML GaP/GaAs(110) (the dashed line is a guide to the eye). Error bars indicate the range of areal densities measured at several positions across each sample.

Overall, more nanostructure nucleation events will hence occur and so the areal density increases, giving the same trend that we see in Fig. 7. So, even though the study of tensile self-assembly is still in its infancy, it appears that many of the kinetic theories underpinning traditional compressive self-assembly still apply.

C. Adatom diffusion length and tensile-strained self-assembly

Although similarities exist between tensile-strained self-assembly on GaAs(110) and GaAs(111)A, a comparison of samples with similar GaP thicknesses shows that surface orientation nevertheless has a strong influence on nanostructure morphology and distribution [Figs. 6(a)–6(d), respectively]. The surface diffusion length of Ga adatoms (λ_{Ga}) on GaAs is known to be highly orientation-dependent, such that $\lambda_{\text{Ga}}(110) > \lambda_{\text{Ga}}(111)\text{B} > \lambda_{\text{Ga}}(111)\text{A} > \lambda_{\text{Ga}}(001)$.²⁶ We suggest that this inequality in λ_{Ga} lies at the heart of the differences we observe in the position, shape, size, and areal density of the GaP nanostructures on GaAs(110) and GaAs(111)A [Fig. 6].

On GaAs(110), the GaP nanostructures tend to form solely at step-edges [Fig. 8(a)].⁶ Although intensity modulation in the fast Fourier transform (FFT) of the AFM image [inset of Fig. 8(a)] is weak due to the low areal density of the nanostructures, there is still evidence for ordering parallel to the step-edges. For the growth conditions used, $\lambda_{\text{Ga}}(110)$ is longer than the average terrace width on the GaAs(110)

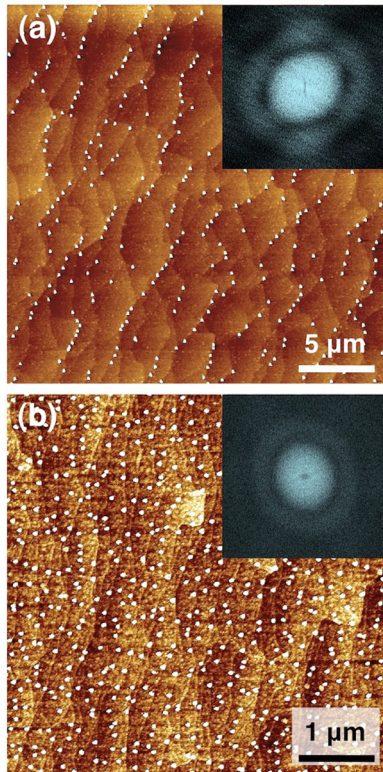


FIG. 8. (a) $625 \mu\text{m}^2$ AFM image of 6.4 ML GaP/GaAs(110), showing nanostructure ordering along the buffer step-edges. (b) $25 \mu\text{m}^2$ AFM image of 1.7 ML GaP/GaAs(111)A, showing random nanostructure location across the buffer surface (note the different scale in (a) and (b)). Insets to (a) and (b) are fast Fourier transforms of the two images.

buffer and hence the step-edges mediate nanostructure nucleation.⁶ In contrast, despite the ready availability of step-edges on GaAs(111)A, GaP nanostructures nucleate randomly across the surface [Fig. 8(b)].⁷ The FFT of this image [inset of Fig. 8(b)] confirms the isotropic location of nanostructures on GaP/GaAs(111)A and demonstrates that most nanostructures nucleate before the adatoms reach the step-edges. Although a higher T_{sub} is required for GaP/GaAs self-assembly on (111)A compared with (110) ($\geq 520^\circ\text{C}$ and 460°C , respectively), $\lambda_{\text{Ga}}(111)\text{A}$ is still apparently lower than the average terrace width.

The elongated, pyramidal shape of the nanostructures formed on (110) surfaces [Figs. 6(a) and 6(c)] may also result from a large $\lambda_{\text{Ga}}(110)$, combined with the known anisotropy of the GaAs(110) surface.⁴ The tensile GaP/GaAs(110) features are almost identical to compressive InGaAs quantum dots formed by droplet epitaxy on GaAs(311)A,²⁸ for which the pyramidal shape was attributed to strongly anisotropic surface diffusion.²⁸ In keeping with our previous work,⁶ we note here that the tensile GaP nanostructures formed are free from dislocations and coherently strained with the underlying GaAs(110) surface. The lack of contrast modulation in XTEM [Fig. 9(a)] implies elastic deformation without the creation of dislocations. That strain relief occurs via elastic deformation agrees with the analysis in Sec. II C and supports our conjecture that $E_{\text{nuc}60^\circ}$ is large in tensile-strained materials on (110) surfaces.

In contrast to the (110) surface, the GaP/GaAs(111)A nanostructures are more regular in shape [Figs. 6(b) and 6(d)]. Following nucleation, the GaP/GaAs(111)A nanostructures grow radially due to isotropic adatom diffusion and incorporation. The result is the pseudo-triangular final shape of the GaP/GaAs(111)A nanostructures, which reflects the three-fold symmetry of the underlying substrate. XTEM reveals that the atomic rows extend continuously from the GaAs(111)A buffer into the GaP nanostructure without dislocation formation [Fig. 9(b)]. Elastic deformation by dislocation-free self-assembly is again consistent with Sec. II C which predicts a large $E_{\text{nuc}60^\circ}$ in tensile-strained materials on (111) surfaces.

In self-assembled material systems for which adatom desorption is negligible, nanostructure size and areal density are inversely related.⁴ During GaP/GaAs(111)A growth for example, an increase in T_{sub} results in the formation of larger nanostructures with a corresponding reduction in their areal density.⁷ Raising T_{sub} increases λ_{Ga} . A larger λ_{Ga} in turn encourages the formation of large, low-density nanostructures

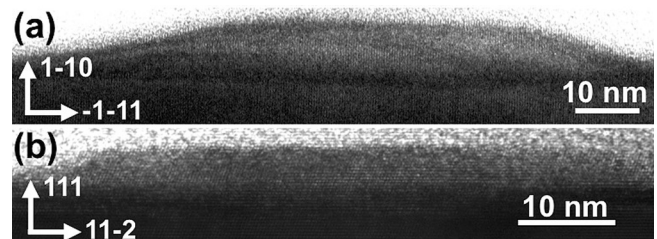


FIG. 9. XTEM of (a) a single 0.7 ML GaP/GaAs(110) nanostructure and (b) a single 1.73 ML GaP/GaAs(111)A nanostructure.

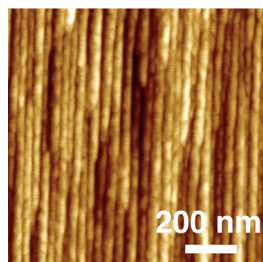


FIG. 10. $1\ \mu\text{m}^2$ AFM image of 4.5 ML GaP grown on 2° off-cut GaAs(111)B. The z-scale is 3 nm.

that minimize strain energy more efficiently than numerous smaller nanostructures.⁴ The nanostructures in Fig. 8(a) are larger and lower density than in Fig. 8(b) (note the difference in scale) providing further support for the inequality $\lambda_{\text{Ga}(110)} > \lambda_{\text{Ga}(111)\text{A}}$.²⁶

D. Tensile-strained growth on GaAs(111)B

Comparing Fig. 4(d) and Fig. 10 shows that GaP deposited onto off-cut GaAs(111)B self-assembles into one-dimensional nanoscale “wires” decorating each terrace on the buffer surface. The Ga adatom diffusion length is lower on GaAs(111)B than GaAs(110).²⁶ Nevertheless, the low average terrace width created by the Ga(111)B substrate misorientation means that similar to the GaP/GaAs(110) samples, step-edges play an important role as barriers to adatom migration between adjacent terraces.²⁹ Surface adatom diffusion is therefore mainly limited to the direction parallel to the step-edges, with the result that continuous nanowires self-assemble. Tensile-strained self-assembly on GaAs(111)B is consistent with the predictions of Sec. II C, although comprehensive analysis with TEM will be required to confirm that the nanowires are dislocation-free. The divergence in self-assembly behavior

between GaAs(111)A and GaAs(111)B buffers may be due in part to the different chemistries of the Ga- and As-terminated surfaces. However, we believe that the main factor influencing the tensile-strained growth behavior on GaAs(111)B is the high step-edge density. In future we will ascertain whether at lower deposition thicknesses we can split the GaP wires into chains of discrete nanostructures, similar to those observed in compressive systems on off-cut (001) substrates.³⁰

V. CONCLUSIONS

We have explored the growth of tensile-strained GaP on the four low-index surfaces of GaAs [Fig. 11]. We describe the MBE growth conditions required to achieve high-quality planar GaAs homoepitaxy for each surface orientation. We present explanations for the striking differences in surface morphology resulting from tensile-strained growth on these four GaAs buffer orientations: the 2D growth mode of GaP/GaAs(001) [Fig. 11(a)], and the self-assembly of 3D GaP nanostructures on GaAs(110) and (111) [Figs. 11(b)–11(d)]. The kinetics underpinning several aspects of tensile-strained self-assembly appear to be consistent with those established for traditional, compressively strained self-assembly. Differences in tensile-strained self-assembly between the (110) and (111)A surfaces are due to unequal adatom diffusion lengths on the two surfaces. In the future we anticipate that tensile-strained self-assembly will be used to access the hitherto unexplored properties of nanostructures and quantum dots on (110) and (111) surfaces.

The authors would like to thank Christopher Yerino for valuable technical assistance.

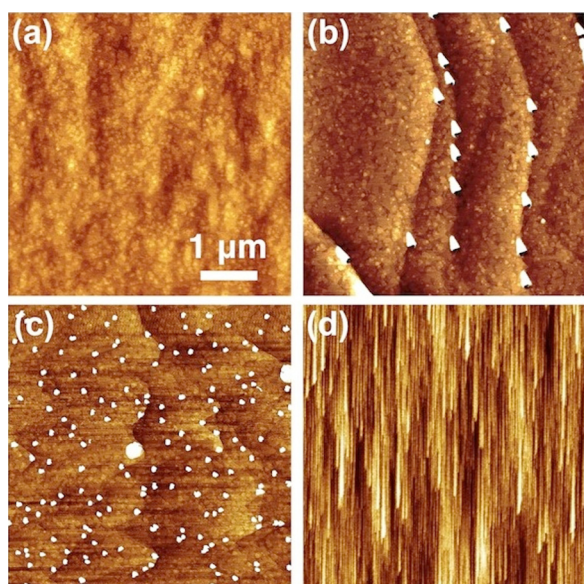


FIG. 11. $25\ \mu\text{m}^2$ AFM images summarizing the different surface morphologies that result from deposition of tensile-strained GaP on the four low-index orientations of GaAs. (a) 4.5 ML GaP/GaAs(001) (z-scale = 3 nm), (b) 4.2 ML GaP/GaAs(110) (z-scale = 3 nm), (c) 1.7 ML GaP/GaAs(111)A (z-scale = 5 nm), and (d) 3.9 ML GaP/GaAs(111)B off-cut by 2° (z-scale = 5 nm).

¹J. Tersoff and F. K. LeGoues, *Phys. Rev. Lett.* **72**, 3570 (1994).

²J. Simon, S. Tomasulo, P. J. Simmonds, M. Romero, and M. L. Lee, *J. Appl. Phys.* **109**, 013708 (2011).

³D. Leonard, M. Krishnamurthy, C. M. Reaves, S. P. Denbaars, and P. M. Petroff, *Appl. Phys. Lett.* **63**, 3203 (1993).

⁴B. A. Joyce and D. D. Vvedensky, *Mater. Sci. Eng. R: Rep.* **46**, 127 (2004).

⁵D. J. Eaglesham and M. Cerullo, *Phys. Rev. Lett.* **64**, 1943 (1990).

⁶P. J. Simmonds and M. L. Lee, *Appl. Phys. Lett.* **97**, 153101 (2010).

⁷P. J. Simmonds and M. L. Lee, *Appl. Phys. Lett.* **99**, 123111 (2011).

⁸D. Pachinger, H. Groiss, H. Lichtenberger, J. Stangl, G. Hesser, and F. Schäffler, *Appl. Phys. Lett.* **91**, 233106 (2007).

⁹E. P. Kvam and R. Hull, *J. Appl. Phys.* **73**, 7407 (1993).

¹⁰J. P. Hirth and J. Lothe, *Theory of Dislocations*, 1st ed. (McGraw-Hill, New York, 1968), p. 780.

¹¹N. Thompson, *Proc. Phys. Soc. B* **66**, 481 (1953).

¹²P. M. J. Marée, J. C. Barbour, J. F. van der Veen, K. L. Kavanagh, C. W. T. Bulle-Lieuwma, and M. P. A. Vieggers, *J. Appl. Phys.* **62**, 4413 (1987).

¹³W. Wegscheider and H. Cerva, *J. Vac. Sci. Technol. B* **11**, 1056 (1993).

¹⁴E. A. Fitzgerald, *Mater. Sci. Rep.* **7**, 87 (1991).

¹⁵K. Sato, M. R. Fahy, and B. A. Joyce, *Surf. Sci.* **315**, 105 (1994).

¹⁶L. Pfeiffer, H. L. Störmer, K. West, and K. W. Baldwin, *J. Cryst. Growth* **111**, 333 (1991).

¹⁷M. Yoshita, H. Akiyama, L. N. Pfeiffer, and K. W. West, *J. Appl. Phys.* **101**, 103541 (2007).

¹⁸D. A. Woolf, D. I. Westwood, and R. H. Williams, *Semicond. Sci. Technol.* **8**, 1075 (1993).

¹⁹A. Chin, P. Martin, P. Ho, J. Ballingall, T.-H. Yu, and J. Mazurowski, *Appl. Phys. Lett.* **59**, 1899 (1991).

²⁰J. W. Cahn and R. E. Hanneman, *Surf. Sci.* **1**, 387 (1964).

²¹D. Leonard, K. Pond, and P. M. Petroff, *Phys. Rev. B* **50**, 11687 (1994).

- ²²A. Raviswaran, C.-P. Liu, J. Kim, D. G. Cahill, and J. M. Gibson, *Phys. Rev. B* **63**, 125314 (2001).
- ²³T. J. Krzyzewski and T. S. Jones, *J. Appl. Phys.* **96**, 668 (2004).
- ²⁴T. Yang, J. Tatebayashi, S. Tsukamoto, M. Nishioka, and Y. Arakawa, *Appl. Phys. Lett.* **84**, 2817 (2004).
- ²⁵W.-H. Chang, W.-Y. Chen, H.-S. Chang, T.-P. Hsieh, J.-I. Chyi, and T.-M. Hsu, *Phys. Rev. Lett.* **96**, 117401 (2006).
- ²⁶T. Takebe, M. Fujii, T. Yamamoto, K. Fujita, and T. Watanabe, *J. Appl. Phys.* **81**, 7273 (1997).
- ²⁷P. B. Joyce, T. J. Krzyzewski, G. R. Bell, T. S. Jones, S. Malik, D. Childs, and R. Murray, *Phys. Rev. B* **62**, 10891 (2000).
- ²⁸J. H. Lee, Z. M. Wang, E. S. Kim, N. Y. Kim, S. H. Park, and G. J. Salamo, *Phys. Status Solidi (a)* **207**, 348 (2010).
- ²⁹V. G. Talalaev, B. V. Novikov, S. Y. Verbin, A. B. Novikov, D. Son Thath, I. V. Shchur, G. Gobsch, R. Goldhahn, N. Stein, A. Golombek, G. E. Tsyrlin, V. N. Petrov, V. M. Ustinov, A. E. Zhukov, and A. Y. Egorov, *Semiconductors* **34**, 453 (2000).
- ³⁰N. Ikoma and S. Ohkouchi, *Jpn. J. Appl. Phys.* **34**, L724 (1995).